Journal of Materials Science: Materials in Engineering

ORIGINAL PAPER

Open Access

Influence of temperature on the compression properties of expanded thermoplastic polyurethane (ETPU)

Johannes Meuchelböck[1], Carlo Peiffer[2], Lena Walter[1], Marcel Dippold[1], Peter Munro[2] and Holger Ruckdäschel[1*]

Abstract

This study explores how expanded thermoplastic polyurethane (ETPU) responds to temperature and compression at various temperatures. Dynamic mechanical thermal analysis (DMTA) was used to understand the temperature influence at small deformations. To investigate the deformation behavior at different compression stages we employed in-situ CT measurements and 3D strain mapping. Through quasi-static compression tests at temperatures from − 50 to 120 °C, we determined the influence of temperature on compression modulus, elastic stress, stress at 50% deformation, densification, and energy absorption. Remarkably, ETPU demonstrates robust recovery after compression, particularly within the − 50 to 60 °C temperature range. Subsequent compression tests show consistent or even slightly increased compression properties, such as a 10% increase in energy absorption for samples previously tested at − 40 °C, indicating that ETPU can withstand prior exposure to different temperatures.

Keywords Elastic polymer, Bead foam, Mechanical compression properties, Temperature influence, Material resilience

Introduction

Expanded thermoplastic polyurethane (ETPU) has gained widespread recognition, notably for its application as the midsole material in Adidas Boost shoes. The commercial success of ETPU stems from its unique blend of ease of processing and exceptional elasticity under high deformation (BASF SE 2024).

Bead foam components are commonly produced through a three-step procedure, starting with the fabrication of the base polymer. Subsequently, the polymer is transformed into expanded beads using either an autoclave or extrusion foaming method. Finally, these expanded beads are welded together to create the end product (Brütting et al. 2023; Raps et al. 2014). This results in a multi-scale morphology that is crucial in defining both the material's structure and its mechanical response (Koch et al. 2023; Gebhart et al. 2019; Meuchelböck et al. 2023).

The mechanical properties of foams are influenced by the base material, its cellular structure, and foam density (Ashby 2006). However, the mechanical behavior of polymer foams varies with temperature, reflecting the temperature-dependent properties of the solid material (Gibson and Ashby 2014). Therefore, foams respond differently under varying temperature conditions. Given the frequent use of bead foams in environments with varying temperature conditions, this topic has significant relevance (Morton et al. 2020; Weingart et al. 2020; Himmelsbach et al. 2022).

Krundaeva et al. demonstrated that temperature has a significant impact on the dynamic compression characteristics of EPS foam. Specifically, it was observed that

*Correspondence:
Holger Ruckdäschel
holger.ruckdaeschel@uni-bayreuth.de
[1] Department of Polymer Engineering, University of Bayreuth, Universitätsstr. 30, Bayreuth 95447, Germany
[2] Department of Medical Physics and Biomedical Engineering, University College London, Gower Street, London WC1E 6BT, UK

the compressive strength of the EPS foam decreased by approximately 13% when the temperature was increased to 50 °C. Conversely, a decrease in temperature to − 20 °C resulted in an 8% increase in the strength of the EPS foam (Krundaeva et al. 2016).

Morton et al. delves into the compression characteristics of EPP for car applications across a temperature spectrum spanning from − 30 to 60 °C. Their findings revealed a 110% increase in collapse stress, representing the transition point from the linear-elastic to plateau regime, at − 30 °C. Conversely, at 60 °C, there was a notable 50% decrease in this collapse stress when compared to the reference temperature of 23 °C (Morton et al. 2020).

Weingart et al. conducted a comparative analysis, assessing the mechanical performance of expanded polycarbonate (EPC) alongside expanded polypropylene (EPP) and expanded polyethylene terephthalate (EPET) at different ambient temperatures (25 °C, 80 °C, and 200 °C). Notably, compression, tensile, and flexural properties exhibited substantial reductions when increasing the temperature. For instance, EPP experienced a 45% decrease in tensile strength at 80 °C and a 61% decrease at 110 °C. In summary, the resistance of all three bead foams is decreased at higher temperatures. However, EPC demonstrated the least deterioration in mechanical performance, likely attributable to the superior temperature resistance of the solid PC material compared to PP and PET (Weingart et al. 2020).

Currently, research on the temperature-dependent behavior of ETPU is limited. Existing studies focussing on the autoclave process of ETPU indicate that higher saturation temperatures lead to more expansion, while increased pressure results in smaller cells; higher temperature at the same pressure creates larger cells (Zhao et al. 2018; Zhang et al. 2017). However, the TPU composition is crucial too. Zhang et al. found that a higher molecular weight of TPU's soft segment affects foaming (Zhang et al. 2017). Saturation temperature and pressure significantly affect foam morphology by influencing the ordering of TPU's hard segments in a highly elastic state, which is crucial for autoclave foaming and inter-bead bonding in welding (Jiang et al. 2021).

The structure of ETPU affects its deformation behavior. Singaravelu et al. demonstrated through in-situ X-ray microtomography that the compression behavior of ETPU bead foams is closely linked to its structure, with strain mapping underscoring how cellular irregularities affect local stability and void collapse. Additionally, they found that differences in ligament thickness and material distribution critically impact the mechanical response, leading to varied Poisson ratios in both individual expanded beads and molded plates (Singaravelu et al. 2019, 2021).

Ge et al. conducted a study that not only revealed a significant enhancement in the tensile and compression properties of ETPU with increased density but also showcased the impressive recovery capability of ETPU bead foam. Even after subjecting the material to 200-fold loading at 60% strain and allowing a recovery period of 6 days, only marginal decreases were observed in both compression modulus and stress at 60% strain (Ge et al. 2017). Compared to EPP, ETPU shows a very high resistance against cyclic-dynamic load (Meuchelböck et al. 2023). This robust fatigue behavior, in conjunction with its resilience in recovery, highlights ETPU's suitability for applications requiring extended durability under cyclic loading (Ge et al. 2017; Meuchelböck et al. 2023).

Prior research on compact TPU reveals that temperature significantly influences the mechanical behavior of this elastic material. Slater et al. examined the alteration of compression set at various temperatures (23 °C, 50 °C, 70 °C, 80 °C) and observed a substantial increase from up to approx. 40% at 80 °C compared to 23 °C (Slater et al. 2011). Boubakri et al. illustrated the significant impact of temperature on TPU's tensile properties. For instance, aging TPU at 70 °C for 60 days led to an increased modulus and increased tensile stress at 200% elongation (Boubakri et al. 2011). Kasgoz et al. demonstrated that slight temperature variations significantly impact TPU's mechanical response. The tensile modulus decreased by approximately 50%, transitioning from 0.063 MPa at 30 °C to 0.030 MPa at 40 °C and 0.020 MPa at 50 °C. These changes occurred after thermal conditioning of the samples at their respective temperatures for 10 min (Kasgoz 2021).

In this study, we utilize 3D strain mapping to analyze deformation behavior and perform quasi-static tests on a commercially available ETPU grade at varying densities. This research covers a broad temperature range (− 50 to 120 °C) to evaluate its influence on compression properties. Our goal is to deepen the understanding of ETPU's mechanical behavior, inspiring product enhancements and facilitating innovative applications.

Methods

To minimize manufacturing effects, we utilized commercial ETPU expanded beads (Infinergy® 32-100 U10, BASF SE). These beads were welded to plates measuring 290 * 190 * 40 mm^3 using a steam chest molding machine (Energy Foamer 5.0, Kurtz Ersa), with welding parameters based on the provided data sheet specifications. Three density ranges were produced by varying the crack distance during mold filling according to the datasheet (BASF SE 2024).

Subsequently, circular samples with 20 mm and 40 mm diameters were precision-cut from the plates using

a water jet cutting device (Flow Mach 2). Afterwards, the samples were carefully separated from the plates using a cutter knife. For 20-mm diameter samples, the foam skin was removed on both sides, resulting in a 20-mm height without foam skin. After a minimum 144-h conditioning period at 23 °C and 50% relative humidity, the geometric density of each sample was determined (Fig. 1).

Morphology

To analyze the morphology of ETPU expanded beads, ten beads were longitudinally cut using textile scissors and examined with a scanning electron microscope (Zeiss Leo 1530, operating at 1.5 kV acceleration voltage). Due to the varied morphology of the beads, three distinct zones were visually identified for each bead, as illustrated in Fig. 2. The mean cell diameter was calculated with ImageJ by measuring the largest and smallest diameter of the cells. Within the inner circle K1, all complete cells are measured. Circle K2 is divided into four segments, while Circle K3 entails measuring all cells from one-eighth.

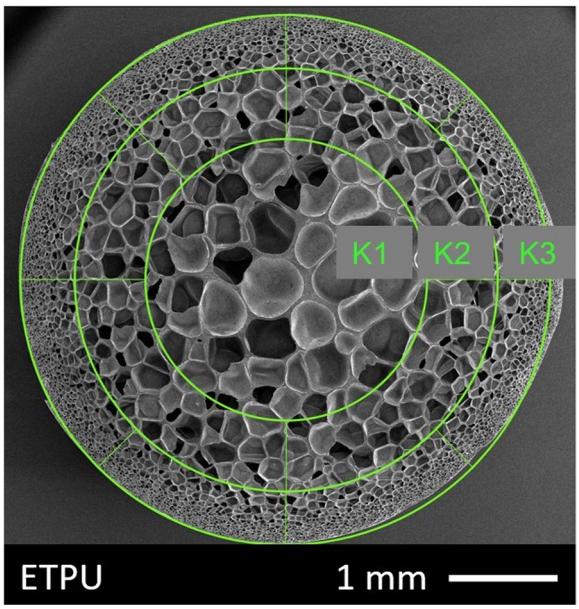

Fig. 2 Three zones of expanded bead morphology, labeled K1, K2, and K3, progressing from center to bead wall

Density

The density ρ_A of 100 beads was determined using Archimedes' principle and a density scale (Mettler Toledo AG245), with m_{air} representing the mass of the bead in air, m_{H2O} as the apparent mass of the bead under water, and $\rho_{\text{H}_2\text{O}}$ denoting the density of water at the measurement temperature (25 °C) in Eq. 1.

$$\rho_A = \frac{m_{air}}{m_{air} - m_{H_2O}} * \rho_{H_2O} \tag{1}$$

The geometric density ρ of the test samples for DMTA and compression tests are calculated according to Eq. 2.

$$\rho = \frac{m}{V} \tag{2}$$

The mass m and volume V of the cylindrical samples are determined after a conditioning period of at least 144 h at laboratory conditions. The volume of the cylindrical sample is calculated using the height and diameter as the mean values obtained from measurements at three different positions.

Strain mapping using edge illumination

In order to investigate the deformation behavior, 3D-strain maps were generated at deformation levels between 2 and 5%, 30 and 35%, and 55 and 60%. Edge-illumination (EI) phase contrast imaging (Olivo 2021) was used as the primary imaging technique and strain retrieval was conducted using the commercial digital volume correlation (DVC) software package in AVIZO. For each loading condition, 1000 phase enhanced projections were obtained by applying the single shot phase retrieval method (Diemoz et al. 2017) on the raw projection images. A CT reconstruction was then performed using the vector geometry and the Feldkamp-Davis-Kress reconstruction algorithm from the ASTRA toolbox (van Aarle et al. 2016).

When using DVC, one has to make a trade-off between strain uncertainty and strain spatial resolution. The strain uncertainty depends on the characteristics of the primary imaging method and on the sample features, and generally increases for finer meshes. A zero-strain uncertainty

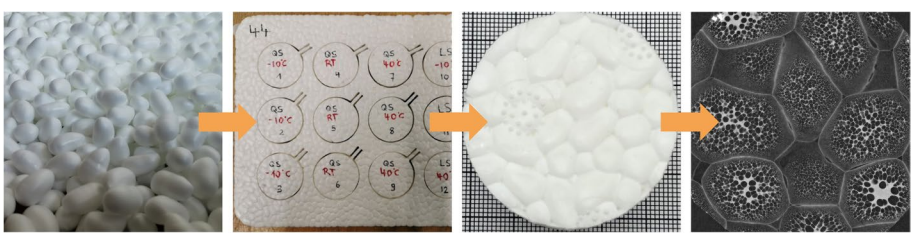

Fig. 1 From ETPU expanded beads to sample, with an exemplary CT-image of the cross-section

measurement (Bay et al. 1999) was conducted, where two repeat scans of the sample under no strain were correlated. This was done for different mesh sizes and the standard deviation of the retrieved strain acted as an estimate for the strain uncertainty. The result of this procedure is plotted in Fig. 3. As expected, the uncertainty increases the finer the mesh size is chosen. For this study an average cell size of 20 voxels was chosen because overall strains of 3–5% were applied and therefore a standard deviation of ≈0.06% is still acceptable. Smaller meshes were not considered because the DVC algorithm did not converge. A more detailed description of the X-ray imaging system and the compression test procedure can be found in the supporting information section.

Segmentation of individual ETPU cells

In order to investigate the influence of the ETPU cell size on the deformation behavior, single cells were segmented from the 2% deformation EI CT reconstruction. First, thresholding was used to serve as seed for a watershed segmentation algorithm. The resulting connected label field describing all the cells was separated into distinct objects by a random walk distance map. To avoid labels representing noise, labels with a volume below 10 voxels were excluded. Furthermore only labels with a shape factor between 1 and 2 were considered. Since the cells are expected to be spherical, the 10^5 labels with the least anisotropy were chosen. Then using the result of the 3D strain map the average strain for each label was calculated.

Dynamic mechancial analysis

Dynamical mechanical thermal analysis (DMTA) was performed using a DMA (EPLEXOR Gabo, Netzsch, Germany) equipped with a 150 N force cell. Static compression was set at 4% with a dynamic amplitude of ± 1%. Measurements were conducted at a frequency of 1 Hz and a heating rate of 1 K/min from − 80 to 140 °C. The temperature was controlled with a heated oven supplemented by liquid nitrogen. We chose to use DMTA to determine T_g by the maximum loss factor. This helped us identify the temperature ranges for performing the quasi-static tests, following Sircar et al. (1999).

Quasi-static testing

Samples underwent mechanical testing at temperatures ranging from − 50 to 120 °C. Given the varied behavior observed at different temperatures, categorizing the foam as solely "soft" or "hard" based on its glass transition temperature (T_G) was deemed inadequate. To enable a more accurate comparison across temperatures, all samples were tested at each temperature according

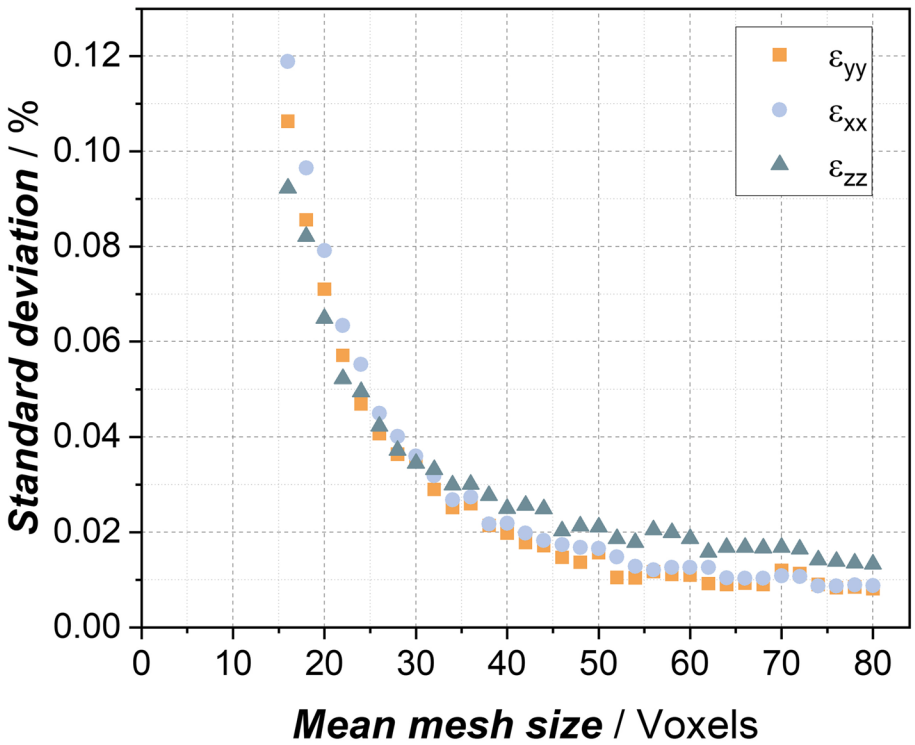

Fig. 3 Standard deviation of the strain for different DVC mesh sizes. The finer the mesh the higher the measured strain uncertainty

to DIN EN ISO 844 standards. According to this standard, the variance for the compression modulus is set at 10%, with a 95% repeatability limit of 25%. We tested at least 3 samples for each density and temperature, for a total of 72 samples. Additionally, to assess the recovery effect, unloading steps were conducted at the same testing speeds.

To ensure that ambient temperature was identical to sample temperature, a dummy sample with the same density was used. A temperature sensor was placed in this dummy sample. Both samples were cooled/heated in the same thermal chamber. When the dummy sample with the same density reached the desired test temperature in the range of ± 2 °C, the test was started. Compression curves were analyzed using the open source Python script by Albuquerque et al. (2023). The methodology for determining the different compression properties is detailed in the cited publication. In essence, the elastic stress is determined at the intersection with a parallel shift by 0.02% from the linear elastic region. The densification strain is identified by the maximum energy absorption efficiency, and the energy absorption is calculated as the area under the compression curve up to the densification strain (Albuquerque et al. 2023).

Results and discussion

Morphology

The morphology and density of the beads were analyzed. The mean density of the analyzed beads is 192 ± 19 kg/m^3. The beads exhibit an ellipsoidal shape with an average principal axis of 9.8 ± 0.4 mm and an average minor axis of 5.9 ± 0.2 mm. To assess the impact of bead density, the average cell diameter of three zones was examined. The results, depicted in Fig. 4, do not show a clear dependency on density. The observation of decreasing cell sizes closer to the bead wall, as shown in Fig. 2, is validated by the measurements. For instance, a bead with a density of 194 kg/m^3 exhibits average cell diameters of 410 µm in zone K1, 231 µm in zone K2, and 71 µm in zone K3. This heterogeneous morphology, as discussed in the introduction, strongly influences single bead deformation (Singaravelu et al. 2021).

Thermal analyis

Figure 5 shows the DMTA results. All densities exhibit a similar pattern, starting with high values that decrease to a plateau before gradually declining further. The storage modulus is consistently higher with increasing density throughout the entire temperature range. The glass transition temperature, as charactarized by the maximum loss factor, occurs around − 25 °C. Below this

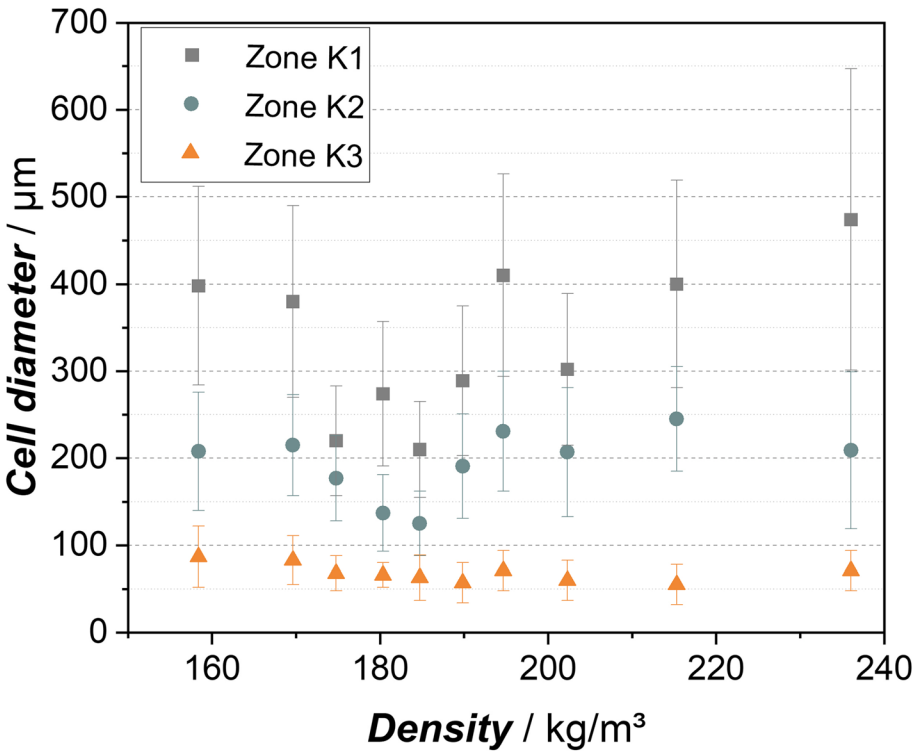

Fig. 4 Equivalent diameter of foam cells from beads with different densities

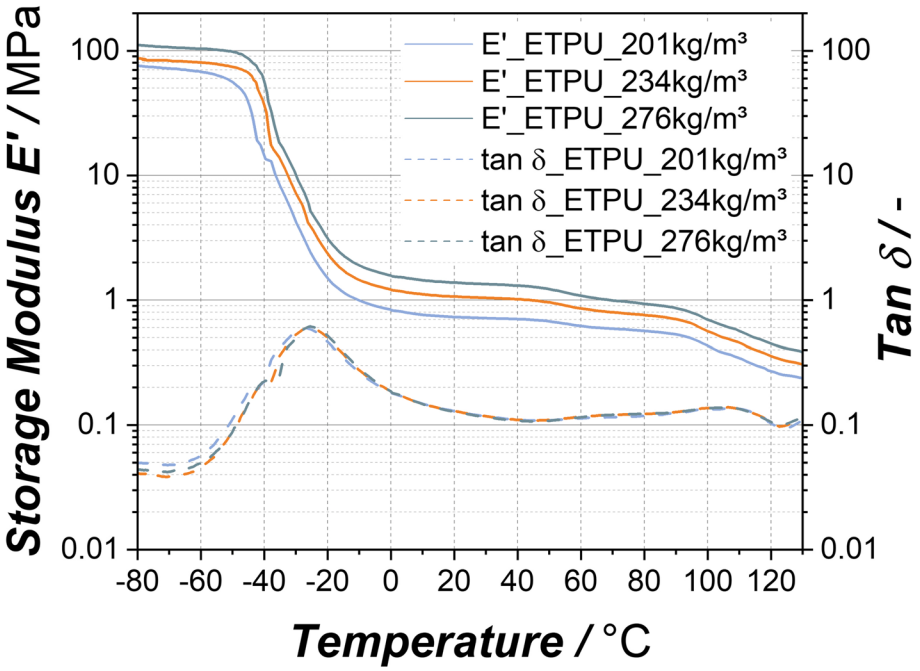

Fig. 5 Results of the DMTA trials: comparison of the storage modulus and loss factor of ETPU with different densities

temperature the material is in a glassy state and starts to soften at around − 45 °C. Following the transition phase, the material enters a rubbery plateau, spanning from approximately 0 °C to 50 °C. Beyond this range, up to around 90 °C, the slope increases as the material enters the rubber flow phase (Sircar et al. 1999).

Deformation behavior

The deformation behavior of foams typically includes three distinct regions: the linear-elastic region, the plateau region, and the densification region, as delineated by Ashby (2006). Gibson et al. classify foams into brittle, plastic-elastic, and elastic categories based on the characteristics of the compressive stress-strain curve (Gibson and Ashby 2014). In Fig. 6, an exemplary compressive stress-strain curve for ETPU with a density of 260 kg/m^3 is presented, demonstrating elastic behavior. Using the analytical approach of Albuquerque et al., the regions are computable (Albuquerque et al. 2023): the linear-elastic region extends up to 4.2%, the plateau spans from 4.2 to 55%, and densification occurs beyond 55% up to the tested 75%. The transition from the linear to the plateau region is gradual and smooth, with the slope-indicative of material stiffness-remaining nearly constant up to the onset of densification. This consistency is crucial for uniform material response throughout a wide deformation range.

During unloading, the material's elasticity is evident, as it only retains about 4% residual strain at the end of the test, utilizing the same testing speed. ETPU can undergo substantial deformation with relatively low stress, a notable characteristic compared to other bead foams like EPP of similar density (Brütting et al. 2023). The compressive stress-strain curves of ETPU create a hysteresis loop, where the area between the loading and unloading curves represents the energy dissipated during deformation. The energy retained in the material, as indicated by the area under the unloading curve, exceeds the energy dissipated during deformation (Lazan 1968). This pattern suggests that ETPU has a high rebound capacity under standard conditions.

To further investigate the deformation strains resulting from compressive forces in the ETPU foam, we conducted 3D strain mapping. The deformation ranges were selected at the transition from the linear to the plateau region, the plateau region and the start of the densification. The results of these trials are visualized in Fig. 7. It is evident that the primary deformation at very small strains occurs primarily at areas around the fusion boundaries of the beads. This suggests that mainly the small cells of zone K3 are deformed (compare Fig. 2). Plotting the equivalent strain against the sphere radius, as shown in Fig. 8, confirms the assumption that the deformation of smaller cells seems greater than that of larger cells.

Between 30 and 35% compression, the deformation of the cells around the fusion boundaries of the beads becomes even more pronounced, making the multiscale structure visible. Finally, at deformations between 55 and

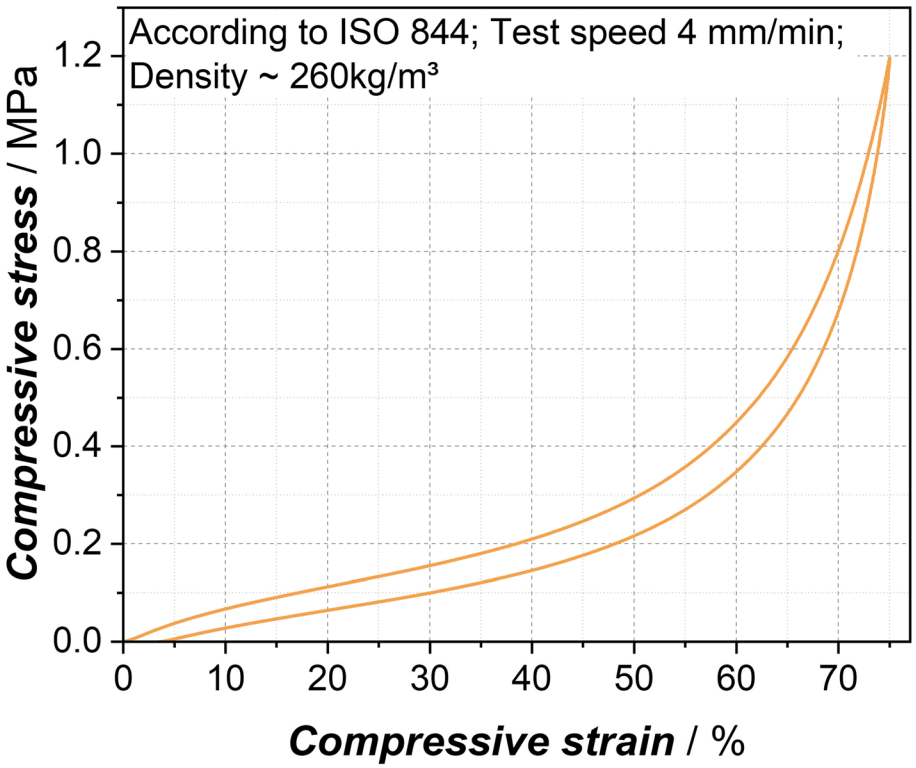

Fig. 6 Compressive stress-strain curve of ETPU sample at 260 kg/m^3, loaded at a testing speed of 4 mm/min up to 75% compression and unloaded down to a residual stress of 0.001 MPa

60% compression, there is a noticeable uniform deformation observed throughout the entire sample.

These findings can guide the design of the cellular structure of ETPU foam. To enhance elasticity at smaller deformations, a heterogeneous structure may be beneficial, featuring smaller cells near the bead walls and larger cells with thicker struts in the center. Conversely, a more uniform structure throughout the beads might help in achieving consistent deformation, reducing the likelihood of weak spots. However, to validate this further, tests with different foam structures are necessary.

Mechanical properties

Results shown in Fig. 7 suggest varying deformation mechanisms depending on the load. ETPU typically experiences greater deformations in its practical applications compared to those observed in DMTA tests (Allen et al. 2020). Consequently, we will discuss the effects of temperature on ETPU deformations up to 75% in the following sections.

The compression test results, depicted in Fig. 9, detail how temperature influences the mechanical behavior of ETPU.

The stress-strain curves in Fig. 9a clearly show that temperature impacts all stages of ETPU deformation. The most significant alterations are observed in tests conducted at temperatures below − 25 °C and above. This is due to ETPU transitioning from a glassy state at temperatures below its glass transition temperature (T_g = − 25 °C, compare Fig. 5) to a rubbery state above it (Sircar et al. 1999).

The temperature-dependent compression properties for ETPU foams of three different densities are presented in Fig. 9b–f. The data indicates that higher density leads to increased compression modulus, elastic stress, stress at 50% deformation, and energy absorption, while densification strain decreases with increasing density.

The compression modulus in Fig. 9b follows a similar pattern as the DMA curve in Fig. 5, with a marked decrease from − 50 to − 20 °C, and a more gradual decrease from − 20 to 40 °C. For instance, an ETPU foam with a density of 250 kg/m^3 exhibits a compression modulus of 1.19 MPa at − 20 °C, 0.87 MPa at 23 °C, and 0.82 MPa at 40 °C. A significant reduction in stiffness is observed at temperatures above 80 °C, demonstrating that ETPU becomes less rigid with increasing temperature.

The elastic stress of ETPU, indicating the onset of the plateau region, rises at lower temperatures but remains

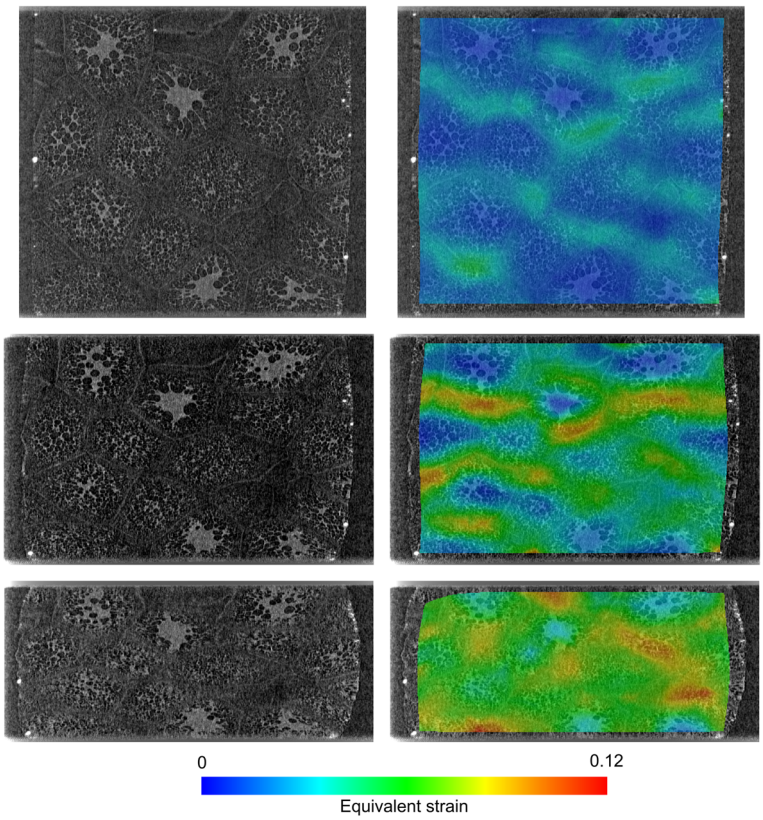

Fig. 7 Visualization of ETPU deformation behavior: The left side shows X-ray CT slices along the compression direction, while the right side shows corresponding slices through the 3D strain maps. From top to bottom, the images sequentially illustrate the linear region (3–5% compression), the plateau region (30–35% compression), and the onset of densification (55–60% compression) in the foam

relatively constant from − 20 to 40 °C, with a slight decrease observed at higher temperatures.

The densification strain, marking the start of densification, is lowest at − 40 °C and increases progressively with temperature. For example, ETPU foam with a density of 253 kg/m^3 has a densification strain of 55% at − 50 °C, 51% at − 40 °C, increasing to 55% at 23 °C, and 58% at 80 °C. Above 80 °C, the increase in densification strain becomes less marked.

The stress required for 50% deformation initially drops sharply below − 25 °C, then stabilizes between − 20 and 40 °C, and decreases more noticeably from 80 to 120 °C, indicating the material softens with temperature.

Energy absorption in ETPU foam is highest at lower temperatures, attributed to its brittleness in a glassy state which could lead to a higher energy dissipation on impact. Above its glass transition temperature, ETPU's elasticity allows to return energy, increasing its versatility. Consequently, ETPU could be an ideal protective layer for tanks containing gases or liquids below − 50 °C. Since the material provides excellent protection against vibrations above − 20 °C without deforming permanently. In the event of gas leaks causing ETPU to freeze, the amount of energy that ETPU can absorb increases.

To assess how temperature impacts recovery, we examined the change in sample height immediately after testing and 24 h after testing at room temperature, as depicted in Fig. 10a. Directly after testing, notable deformation is observed, with samples at − 50 °C reaching only 42% of their original height, while those at − 40 °C reach 65%. This suggests a reduction in elasticity at these temperatures, hindering the samples from promptly returning to their original shape with repeated deformations. In the temperature range from − 20 to 60 °C, samples rapidly recover close to 100% of their original height. At higher test temperatures, such as 80 °C and 120 °C, the recovery percentages are 94% and 90%, respectively. The material starts to melt at these temperatures, as evidenced by the increase of the loss factor tan δ from around 50 °C onwards, as shown in Fig. 5.

Allowing the samples to rest at laboratory conditions after testing, reveals that the original height is restored for temperatures ranging from − 50 to 60 °C. Permanent height changes become apparent at higher test temperatures, with 3% at 80 °C and 7% at 120 °C.

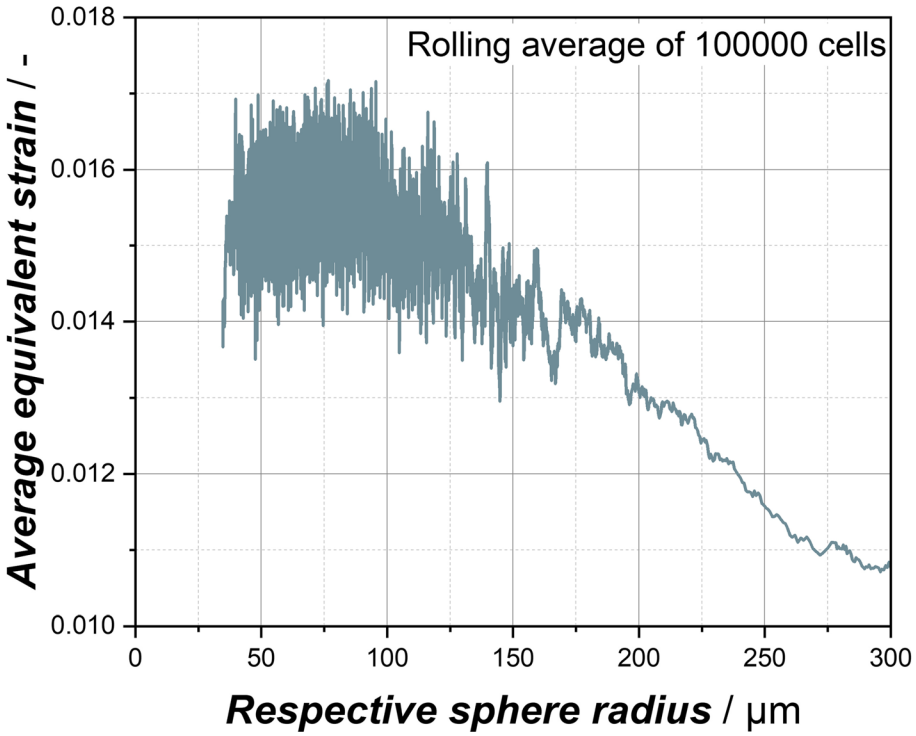

Fig. 8 Rolling average of length 100 of the equivalent strain between 3 and 5% compression of 100,000 cells in relation to their respective sphere radius

The recovery behavior was further examined by analyzing the compression properties of all test series with a second load to 75% deformation at 23 °C, after a 72-h recovery period. The results of this were compared to a sample being compressed only once to 75% deformation at 23 °C. As shown in Fig. 10b, the compression modulus matches or exceeds the initial stiffness. Compressing ETPU to 75% twice at 23 °C does not alter its stiffness, demonstrating its strong elastic behavior. Surprisingly, the material's deformation does not appear to be affected by the test temperature of the initial load. Samples tested at − 50 °C achieve 97% of the stiffness compared to those subjected to the first load at 23 °C. Some samples even exhibit increased stiffness, possibly influenced by the initial load. However, there is no discernible trend correlating with the temperature of the initial load.

Similarly, the energy absorption in Fig. 10c remains consistent with the original values at 23 °C. This suggests that neither property is significantly influenced by initial testing, regardless of the initial temperature. Observing an increased energy absorption at 23 °C suggests a small loss in elasticity during the initial load. Further exploration through dynamic cyclic loading at larger deformations and various temperatures is needed to understand this phenomenon better. However this investigation shows clearly the material's potential to maintain similar shape and compression properties even after being compressed to 75% at different temperatures.

Conclusions

In this study, we investigated the influence of temperature on the compression properties of expanded thermoplastic polyurethane (ETPU) across a wide temperature range (− 50 °C to 120 °C). Our findings provide a comprehensive understanding of ETPU's mechanical performance under various thermal conditions, demonstrating the material's significant versatility and resilience.

DMTA measurements show temperature dependent behavior at different densities. The stiffness decreases drastically at the glass transition temperature (approximately − 25 °C), showing a plateau up to 80 °C before further decreasing.

In-situ CT measurements and 3D strain mapping at different compression levels allow to analyze deformation mechanisms. Depending on the compression level the cellular structure is affected differently. Initially, the deformation is concentrated at the bead borders, with more uniform deformation across the bead walls as the compression increases. These findings unveil paths to tailor the mechanical properties of ETPU by adjusting its cellular structure.

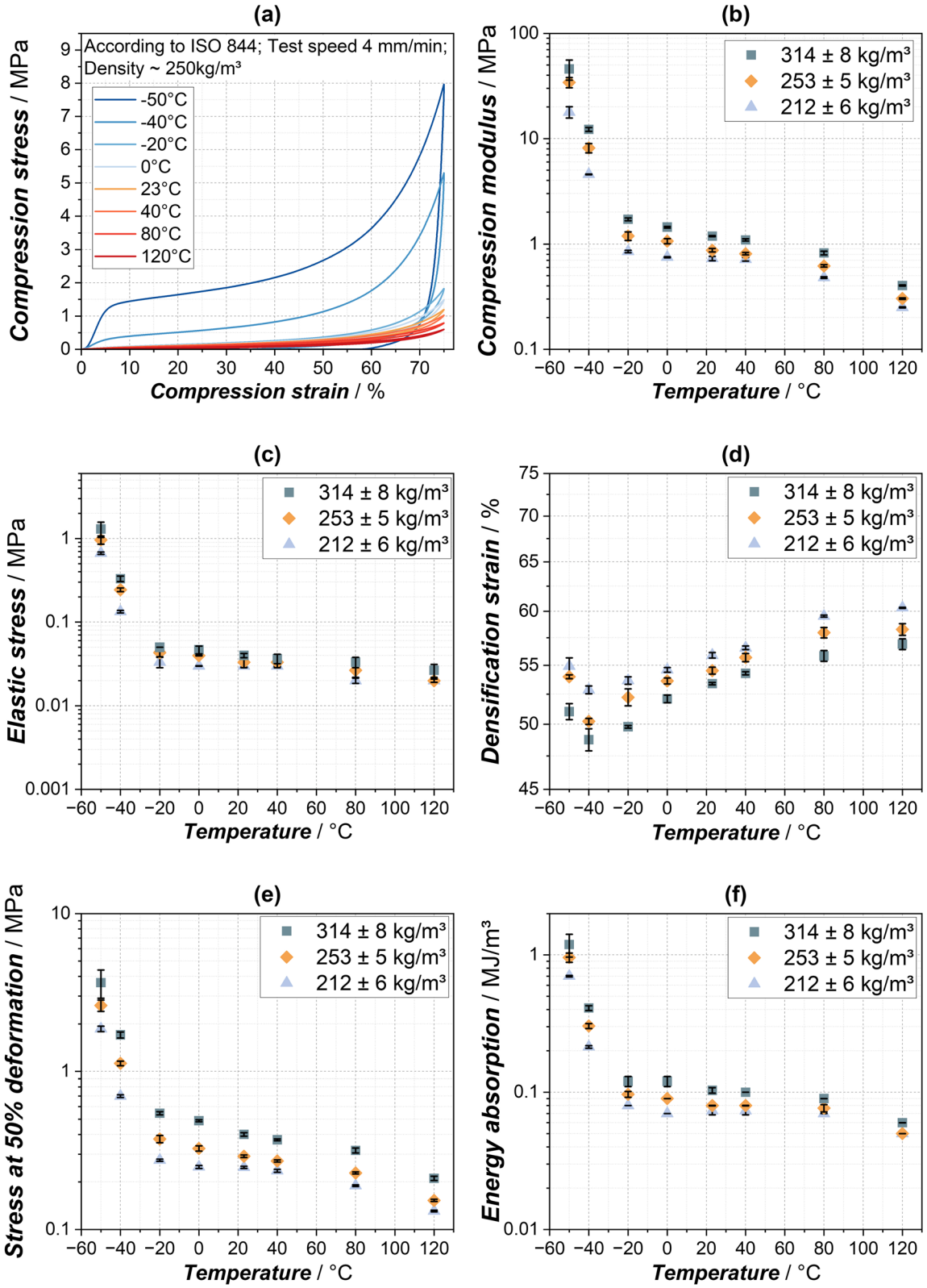

Fig. 9 Visualization of the influence of temperature in **a** representative stress-strain curves, in **b** the compression modulus, in **c** the elastic stress, in **d** the analyzed onset of densification strain, in **e** the compression stress at 50% deformation, and in **f** the energy absorption of the material up to densification

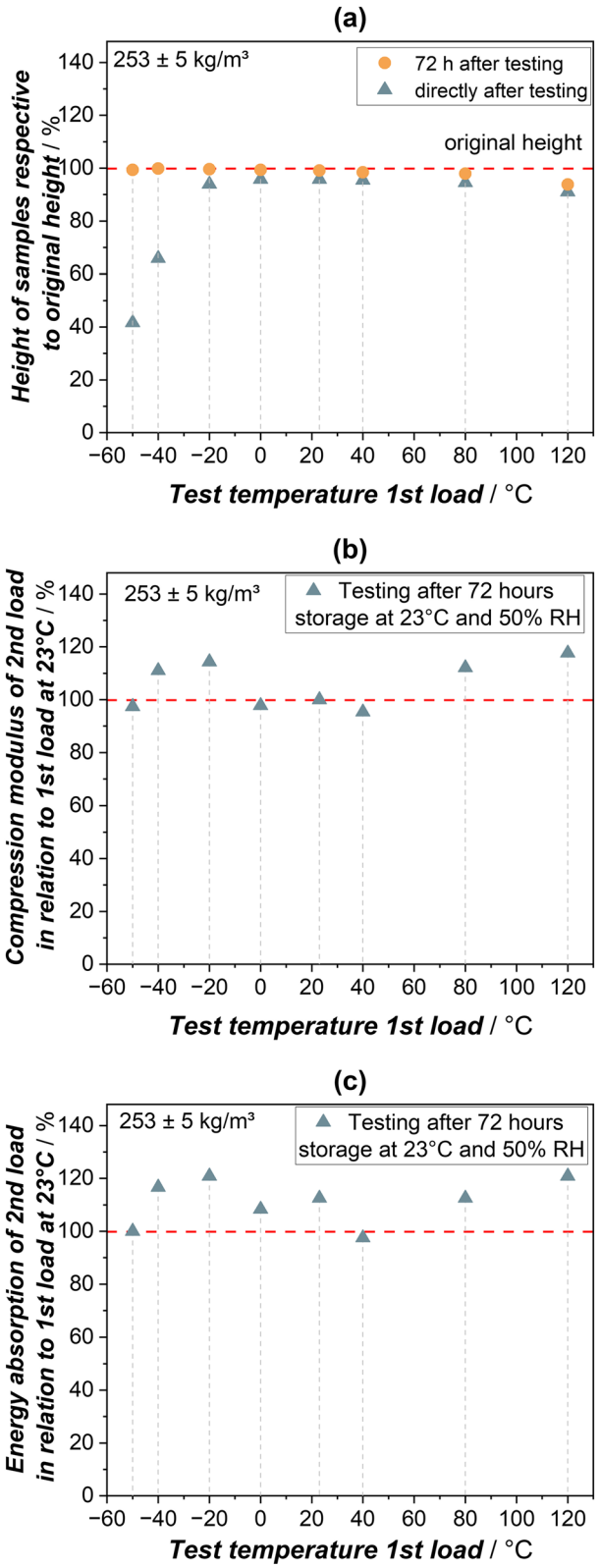

Fig. 10 Comparing ETPU's (253 kg/m^3) temperature-dependent recovery behavior: **a** Percentage of height recovery post-compression, measured immediately and 72 h after testing. **b** Compression modulus, and **c** energy absorption on the second compression at 23 °C, each relative to the properties of samples initially tested at 23 °C

In addition we conducted quasi-static compression tests on ETPU with three different densities up to the high deformation of 75% at temperatures ranging from − 50 to 120 °C. The results show a plateau between − 20 and 60 °C, where the compression modulus, elastic stress and energy absorption decrease very slowly. Density affects performance across all temperatures, with higher density samples showing higher compression modulus, elastic stress, and energy absorption capabilities.

ETPU impressively recovers from compression at temperatures ranging from − 50 to 60 °C. Following a 72-h period at room temperature, the material shows minimal residual deformation. Subsequent compression tests at room temperature reveal that both strength and flexibility are unaffected. Notably, both the compression modulus and energy absorption either match or exceed their initial values, indicating ETPU's resilience and ability to maintain its mechanical properties even after being compressed to 75%.

To better understand ETPU's durability over time, future research should investigate its response to cyclic dynamic loading at high deformations across various temperature conditions.

Acknowledgements
Thank you to Andreas Mainz and Ute Kuhn for helping with the test set up. Thank you to Fabian Hübner for bringing the working groups together. Thank you to BASF SE for providing the material.

Supporting information
The Python script (as a jupyter notebook file) and test input files and folders used in this work are freely accessible in GitHub ("https://github.com/Polymer-Engineering-University-Bayreuth/MechanicalProps_Foams.git"). An online tutorial video is available inside the script.

Edge illumination X-ray imaging
In EI, a set of absorbing masks shape the X-ray beam into beamlets and the signal is obtained by analyzing these beamlets individually. Hence, the resolution in EI is decoupled from the detector pixel size and depends on the aperture size of the used masks which in this experiment was 10 µm. However, when taking a single acquisition, the sampling frequency is limited by the sample mask's pitch which is 79 µm, which means that the image is heavily undersampled. By scanning the sample in sub mask-pitch steps (this is called dithering) through the beamlets, a much higher sampling can be realized. A resolution of ≈10 µm can be achieved while fulfilling the Nyquist sampling condition if 16 dithering steps are combined into one projection image. Typically, increasing the resolution in X-ray imaging comes at the cost of a decreased field of view (FOV), but with EI a comparatively big FOV (≈30 × 30 mm) can be achieved at the comparatively high resolution of 10 µm. Since for this study many CT scans under different loading conditions were taken, only two dithering steps were employed in order to save scanning time.

Compression test series for strain imaging
The ETPU sample was precompressed by 1mm by adjusting a screw of the manual compression stage. Then, using the sample height as reference, the earlier mentioned compression levels were set and a full CT data set was acquired. The sample was given 30 min to relax after each compression step before starting the CT scan to avoid any motion artifacts. Furthermore, the compression level in each regime was increased incrementally so that decorrelation (because of strong local deformations or yielding) between subsequent scans could be avoided. This means that scans were taken at deformation levels of 2%, 3.5%, 5%, 30%, 31.25%, 32.5%, 33.75%, 35%, 55%, 56%, 57%, 58%, 59%, and 60%. In order to map the local strain from the minimum deformation to the maximum deformation of the respective deformation regime, AVIZO's global DVC algorithm was used and a python script was written: For an initial mesh the displacement field of the first loading step is calculated, then the initial mesh is transformed by the calculated displacement field and used as the initial mesh for the next loading step. The displacement fields of each loading step are added and lastly, the strain tensor is calculated from the resulting displacement field. This process was started on a coarse mesh. The resulting displacement fields are then used as initial guesses for the DVC on a refined mesh. This ensures faster and more reliable convergence of the DVC algorithm.

Authors' contributions
JM: writing of the original draft, experimental setup and measurements preparation of the compression tests, discussion; CP: experimental setup and measurements preparation of the strain mapping, discussion, paper correction; LW: compression testing, discussion, paper correction; MD: discussion, paper correction; PM: discussion, paper correction, supervision; HR: discussion, paper correction, supervision; all authors read and approved the final manuscript.

Funding
Open Access funding enabled and organized by Projekt DEAL. This publication received funding from DFG project number 437872031, from the Engineering and Physical Sciences Research Council grants EP/T005408/1 and EP/P005209/1 and the Royal Society. Open Access funding enabled and organized by Projekt DEAL. We extend our sincere gratitude for the financial support provided.

Availability of data and materials
The datasets used and/or analyzed during the current study are available from the corresponding author on reasonable request.

Declarations

Ethics approval and consent to participate
Not applicable.

Competing interests
The authors declare that they have no competing interests.

Received: 30 April 2024 Accepted: 2 July 2024
Published online: 16 July 2024

References

Albuquerque RQ, Meuchelböck J, Ruckdäschel H (2023) A unified approach for evaluating mechanical compression tests for polymer bead foams. J Process Eng. https://doi.org/10.1002/pol.20230704

Allen T, Pagan M, Martin R, Duncan O (2020) Effect of rest periods on mechanical ageing of running shoes. In: The 13th Conference of the International Sports Engineering Association. MDPI, Basel, p 138. https://doi.org/10.3390/proceedings2020049138

Ashby MF (2006) The properties of foams and lattices. Phil Trans R Soc A Math Phys Eng Sci 364(1838):15–30. https://doi.org/10.1098/rsta.2005.1678

BASF SE (2024) Infinergy® – superelastic foam for lightweight running shoes. https://www.basf.com/global/en/who-we-are/innovation/our-innovations/superelastic-foam-for-running-shoes.html. Accessed 2024

Bay BK, Smith TS, Fyhrie DP, Saad M (1999) Digital volume correlation: Three-dimensional strain mapping using x-ray tomography. Exp Mech 39:217–226

Boubakri A, Haddar N, Elleuch K, Bienvenu Y (2011) Influence of thermal aging on tensile and creep behavior of thermoplastic polyurethane. Compt Rendus Mécanique 339(10):666–673. https://doi.org/10.1016/j.crme.2011.07.003

Brütting C, Standau T, Meuchelböck J, Schreier P, Ruckdäschel H (2023) A review on semi-crystalline polymer bead foams from stirring autoclave: processing and properties. E-Polymers 23(1). https://doi.org/10.1515/epoly-2023-0092

Diemoz PC, Hagen CK, Endrizzi M, Minuti M, Bellazzini R, Urbani L, Coppi P, Olivo A (2017) Single-shot x-ray phase-contrast computed tomography with nonmicrofocal laboratory sources. Phys Rev Appl 7. https://doi.org/10.1103/PhysRevApplied.7.044029

Ge C, Ren Q, Wang S, Zheng W, Zhai W, Park CB (2017) Steam-chest molding of expanded thermoplastic polyurethane bead foams and their mechanical properties. Chem Eng Sci 174:337–346. https://doi.org/10.1016/j.ces.2017.09.011

Gebhart TM, Jehnichen D, Koschichow R, Müller M, Göbel M, Geske V, Stegelmann M, Gude M (2019) Multi-scale modelling approach to homogenise the mechanical properties of polymeric closed-cell bead foams. Int J Eng Sci 145:103168. https://doi.org/10.1016/j.ijengsci.2019.103168

Gibson LJ, Ashby MF (2014) Cellular solids: Structure and properties, 2nd edn. Cambridge University Press. https://doi.org/10.1017/CBO9781139878326

Himmelsbach A, Standau T, Meuchelböck J, Altstädt V, Ruckdäschel H (2022) Approach to quantify the resistance of polymeric foams against thermal load under compression. J Polym Eng 42(4):277–287. https://doi.org/10.1515/polyeng-2021-0312

Jiang J, Liu F, Yang X, Xiong Z, Liu H, Xu D, Zhai W (2021) Evolution of ordered structure of tpu in high-elastic state and their influences on the autoclave foaming of tpu and inter-bead bonding of expanded tpu beads. Polymer 228:123872. https://doi.org/10.1016/j.polymer.2021.123872

Kasgoz A (2021) Mechanical, tensile creep and viscoelastic properties of thermoplastic polyurethane/polycarbonate blends. Fibers Polym 22(2):295–305. https://doi.org/10.1007/s12221-021-0113-z

Koch I, Preiß G, Müller-Pabel M, Grüber B, Meuchelböck J, Ruckdäschel H, Gude M (2023) Analysis of density-dependent bead and cell structure of expanded polypropylene bead foams from x-ray computed tomography of different resolution. J Cell Plast 59(2):165–184. https://doi.org/10.1177/0021955X231165343

Krundaeva A, de Bruyne G, Gagliardi F, van Paepegem W (2016) Dynamic compressive strength and crushing properties of expanded polystyrene foam for different strain rates and different temperatures. Polym Test 55:61–68. https://doi.org/10.1016/j.polymertesting.2016.08.005

Lazan BJ (1968) Damping of materials and members in structural mechanics, 1st edn. Pergamon Press, Oxford

Meuchelböck J, Raps D, Brückner A, Altstädt V, Ruckdäschel H (2023) Flexural fatigue behaviour and damage mechanism of polystyrene bead foams–influence of the foam density. Int J Fatigue 108095. https://doi.org/10.1016/j.ijfatigue.2023.108095

Meuchelböck J, Standau T, Preiss G, Müller-Pabel M, Koch I, Grüber B, Gude M, Altstädt V, Ruckdäschel H (2023) Effect of density on the fatigue behaviour of EPP and ETPU bead foams. In: proceedings of the 37th international conference of the polymer processing society (pps-37), AIP Conference Proceedings. AIP Publishing, p 140002. https://doi.org/10.1063/5.0168270

Morton DT, Reyes A, Clausen AH, Hopperstad OS (2020) Mechanical response of low density expanded polypropylene foams in compression and tension at different loading rates and temperatures. Mater Today Commun 23:100917. https://doi.org/10.1016/j.mtcomm.2020.100917

Olivo A (2021) Edge-illumination x-ray phase-contrast imaging. J Phys Condens Matter 33. https://doi.org/10.1088/1361-648X/ac0e6e

Raps D, Köppl T, de Anda AR, Altstädt V (2014) Rheological and crystallisation behaviour of high melt strength polypropylene under gas-loading. Polymer 55(6):1537–1545. https://doi.org/10.1016/j.polymer.2014.01.036

Singaravelu AS, Williams JJ, Walter J, Holmes C, Henderson M, Chawla N (2019) In situ four dimensional (4d) x-ray microtomography of the compressive behavior of etpu foam for high performance footware. Microsc Microanal 25(S2):364–365. https://doi.org/10.1017/s1431927619002551

Singaravelu ASS, Williams JJ, Shevchenko P, Ruppert J, de Carlo F, Henderson M, Holmes C, Chawla N (2021) Poisson's ratio of etpu molded bead foams in compression via in situ synchrotron x-ray microtomography. J Mater Sci 56(22):12920–12935. https://doi.org/10.1007/s10853-021-06103-w

Sircar AK, Galaska ML, Rodrigues S, Chartoff RP (1999) Glass transition of elastomers using thermal analysis techniques. Rubber Chem Technol 72(3):513–552. https://doi.org/10.5254/1.3538816

Slater C, Davis C, Strangwood M (2011) Compression set of thermoplastic polyurethane under different thermal-mechanical-moisture conditions. Polym Degrad Stab 96(12):2139–2144. https://doi.org/10.1016/j.polymdegradstab.2011.09.012

van Aarle W, Palenstijn WJ, Cant J, Janssens E, Bleichrodt F, Dabravolski A, Beenhouwer J, Batenburg KJ, Sijbers J (2016) Fast and flexible x-ray tomography using the astra toolbox. Optics Express

Weingart N, Raps D, Kuhnigk J, Klein A, Altstädt V (2020) Expanded polycarbonate (epc)–a new generation of high-temperature engineering bead foams. Polymers 12(10):2314. https://doi.org/10.3390/polym12102314

Zhang R, Huang K, Hu S, Liu Q, Zhao X, Liu Y (2017) Improved cell morphology and reduced shrinkage ratio of ETPU beads by reactive blending. Polym Test 63:38–46. https://doi.org/10.1016/j.polymertesting.2017.08.007

Zhao D, Wang G, Wang M (2018) Investigation of the effect of foaming process parameters on expanded thermoplastic polyurethane bead foams properties using response surface methodology. J Appl Polym Sci 135(25):46327. https://doi.org/10.1002/app.46327

Publisher's Note